Journal of Advanced Ceramics
2021, **10**(4): 809–819
https://doi.org/10.1007/s40145-021-0474-1
ISSN 2226-4108
CN 10-1154/TQ

Research Article

Structure evolution, dielectric, and conductivity behavior of $(K_{0.5}Na_{0.5})NbO_3$–$Bi(Zn_{2/3}Nb_{1/3})O_3$ ceramics

Tianxiang YAN[a,*], Kaiyuan CHEN[a], Chengqi LI[a], Min LIU[b], Jie WANG[c], Liang FANG[a], Laijun LIU[a]

[a]*College of Mechanical and Control Engineering & College of Materials Science and Engineering, Guilin University of Technology, Guilin 541004, China*
[b]*Institute of Fluid Engineering Equipment, Jiangsu Industrial Technology Research Institute, Jiangsu University, Zhenjiang 212013, China*
[c]*Key Laboratory for RF Circuits and Systems, Ministry of Education & Key Laboratory of Large Scale Integrated Design, Hangzhou Dianzi University, Hangzhou 310018, China*

Received: November 14, 2020; Revised: March 3, 2021; Accepted: March 10, 2021

Abstract: $(1-x)K_{0.5}Na_{0.5}NbO_3$–$xBi(Zn_{2/3}Nb_{1/3})O_3$ ($(1-x)$KNN–xBZN, x = 0.010, 0.015, 0.020, 0.025, and 0.030) lead-free ceramics were fabricated via a traditional solid-state method. The crystal structure, microstructure, dielectric, and conductivity behavior of this system were studied. Combined with X-ray diffraction (XRD) patterns, Rietveld refinement, and dielectric spectroscopy, an orthorhombic phase was determined for x = 0.010, an orthorhombic–tetragonal mixed phase was identified for x = 0.015, and a rhombohedral symmetry appears in $0.020 \leqslant x \leqslant 0.030$. Both 0.98KNN–0.02BZN and 0.975KNN–0.025BZN ceramics exhibit stable permittivity and low dielectric loss tangent (tanδ) in wide temperature ranges owing to the combination of rhombohedral–tetragonal step-like feature and the diffuse phase transition from tetragonal to cubic. The activation energies of dielectric relaxation and conductivity behavior at high temperatures initially decrease slightly, then drop sharply, and finally decline slowly, which could be attributed to microstructure morphologies and the concentration of oxygen vacancies.

Keywords: ceramic; crystal structure; dielectric spectroscopy; oxygen vacancies

1 Introduction

Ceramic capacitors as essential electronic components have been largely applied in a variety of fields such as mobile communication, automotive electronics, and military devices [1,2]. Currently, some extreme working conditions including engine control and oil logging provide the requirement of developing high-temperature ceramic capacitors (HTCC) that can work stably higher than 200 ℃ [3,4]. Unfortunately, the operational temperature of widely used X8R (±15% variation of capacitance from –55 to 150 ℃) ceramic capacitors is only lower than 150 ℃ [5,6]. Meanwhile, miniaturization, high reliability, and environmental friendliness are the development trends of HTCC. Therefore, to meet the demand of practical application, the design of lead-free HTCC ceramics with high permittivity (ε'), good

* Corresponding author.
E-mail: yangtxboy@163.com

high-temperature stability of permittivity, and low dielectric loss tangent (tanδ) has received increasing attention [7–23].

At present, a large number of lead-free HTCC ceramics, such as $BaTiO_3$-based ceramics [12,13], $Bi_{0.5}Na_{0.5}TiO_3$-based ceramics [14,15], and $K_{0.5}Na_{0.5}NbO_3$ (KNN)-based ceramics [16,17] have been proposed. Among them, KNN-based relaxor ceramics by composition engineering are regarded as the promising candidates for satisfying HTCC application [16–18]. Generally, the permittivity of unmodified KNN ceramic is highly temperature dependent due to two shape phase transitions from orthorhombic to tetragonal ($T_{O-T} \approx$ 210 ℃) and tetragonal to cubic ($T_{T-C} \approx$ 420 ℃), respectively [19]. Introducing compositions/dopants into KNN for moving phase transitions or producing a diffuse phase transition is an effective method to improve the temperature stability of permittivity [20–23].

Previous studies have shown that the Bi-based compounds modified KNN ceramics, such as KNN–$BiScO_3$ [21], KNN–$Bi(Zn_{2/3}Nb_{1/3})O_3$ [22], and KNN–$Bi(Cu_{2/3}Nb_{1/3})O_3$ [23], showing the good dielectric properties and temperature stability since the valence electrons of Bi 6s hybridize with O 2p to generate the anti-bonding "lone pair" states. Particularly, $Bi(Zn_{2/3}Nb_{1/3})O_3$ (BZN) doped KNN ceramics exhibited high ε' and low tanδ in a broad operational temperature region, which is highly favorable for the practical application of HTCC [22]. The crystal structure evolution and high-temperature conductivity behavior are both of fundamental interest for understanding dielectric properties of KNN-based materials [7,8]. However, a systematical study of crystal structure evolution is still lacking and the influence of BZN content on high-temperature conductivity behavior is unclear for this system.

In the present work, BZN modified KNN ceramics were fabricated to achieve the promising materials for HTCC application. To better understand dielectric properties of this system, the crystal structure evolution was determined by the X-ray diffraction (XRD) patterns, Rietveld refinement as well as dielectric spectroscopy, and the influence of BZN content on high-temperature conductivity behavior was revealed using the impedance spectroscopy. In addition, dielectric relaxation behavior of this system was analyzed in terms of the deviation degree and modified Curie–Weiss law.

2 Experimental

$(1-x)K_{0.5}Na_{0.5}NbO_3$–$xBi(Zn_{2/3}Nb_{1/3})O_3$ ($(1-x)$KNN–xBZN, x = 0.010, 0.015, 0.020, 0.025, and 0.030) lead-free ceramics were fabricated via a traditional sintering method. The raw oxides and carbonates include Na_2CO_3 (99.99%), K_2CO_3 (99.99%), Nb_2O_5 (99.99%), Bi_2O_3 (99.5%), and ZnO (99.0%) (Shanghai Aladdin Bio-Chem Technology Co., Ltd., China). These powders were first fired to remove moisture at 120 ℃ for 24 h and weighted based on the $(1-x)$KNN–xBZN ratios, then mixed by a ball mill for 6 h and calcined at 900 ℃ for 4 h at a heating rate of 5 ℃/min. Next, the calcined powders were ball re-milled for 6 h, and dried and ground by adding 5 wt% polyvinyl alcohol (PVA) binder. Finally, the obtained powders were pressed to form discs of 10 mm in diameter under about 350 MPa and the discs surrounded with the powders of the same composition were sintered at 1100–1120 ℃ for 4 h at a heating rate of 5 ℃/min in alumina crucible, followed by being cooled down with the furnace.

The diameter of sintered ceramics measured by the vernier caliper is 9.04, 9.05, 9.03, 9.12, and 9.13 mm for x = 0.010, 0.015, 0.020, 0.025, and 0.030, respectively. The density was recorded by the Archimedes method. The room-temperature crystal structure was identified using an automatic diffractometer (X'Pert PRO, PANalytical, the Netherlands) with Cu Kα radiation. The crystalline parameters were calculated by the GSAS software. To observe the surface microstructure, the sintered discs were thermally etched at 1000 ℃ for 30 min and then coated with gold to enhance their conductivity. The microstructure morphologies were gained by a scanning electron microscope (SEM, JSM 6380, Japan). Before dielectric measurement, the discs with x = 0.010, 0.015, 0.020, 0.025, and 0.030 were polished to 0.70, 0.75, 0.73, 0.72, and 0.70 mm in different thicknesses, respectively, and painted with silver paste on both surfaces, and then warmed up to 650 ℃ for 30 min to generate electrodes. The ε', tanδ, and impedance data were collected by the means of an impedance meter (Agilent 4294A, USA) in a frequency range of 40 Hz−1 MHz from room temperature (RT) to 550 ℃.

3 Results and discussion

Figure 1(a) shows the XRD patterns of $(1-x)$KNN–xBZN

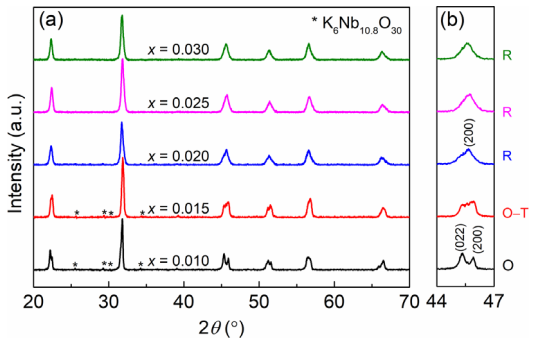

Fig. 1 XRD patterns of (1−*x*)KNN–*x*BZN ceramics with different BZN contents: 2θ (a) from 20° to 70° and (b) from 44° to 47°.

ceramics at RT from 20° to 70°. All samples present a single perovskite structure except that the samples with x = 0.010 and 0.015 include an impurity phase $K_6Nb_{10.8}O_{30}$ (ICDD PDF Card No. 01-070-5051), suggesting that BZN has entered into the lattice to produce a stable solid solution. Moreover, the enlarged XRD patterns from 44° to 47° in Fig. 1(b) show that a trace amount of BZN greatly changes the symmetry of KNN. The peak splitting and higher intensity of (022) peak than that of (200) peak around 45° indicates that the sample with x = 0.010 is an orthorhombic phase (*Amm*2) similar to pure KNN [24]. With increasing BZN, the symmetry for the sample with x = 0.015 changes into an orthorhombic–tetragonal (O–T) mixed phase determined by the intensity of (022)/(002) peak comparable to (200) peak, which is in consistent with the Li-substituted KNN-based solid solution [25]. For the samples with 0.020 ⩽ x ⩽ 0.030, a single (200) peak in the vicinity of 45° suggests the formation of a rhombohedral symmetry (*R*3*m*) since the doping concentration is not very high, and a similar feature can also be observed in the KNN–$(Bi_{0.5}Na_{0.5})ZrO_3$ solid solution [26].

To verify the symmetry and understand the crystal structure evolution of (1–*x*)KNN–*x*BZN ceramics, the Rietveld refinement of XRD data was conducted by the GSAS software [25]. The space groups of all the samples were selected based on the XRD results. The initial crystalline parameters were given according to Ref. [27]. In the process of refinement, the scale factor, background, and cell parameters were revised to minimize the difference between the experimental data and the fitted profile. The refinement results in Fig. 2 show that the experimental data is well fitted. The detailed crystalline parameters, together with R_{wp} (weighted profile residual factor) and R_p (profile residual factor), are listed in Table 1. The reasonable R_{wp} and R_p factors confirm the validation of crystal symmetry.

Figure 2 shows that the unit cell of *Amm*2 includes two octahedral units, whereas one octahedral unit presents in that of *P*4*mm* and *R*3*m*. According to the cell volumes in Table 2, the average volume of

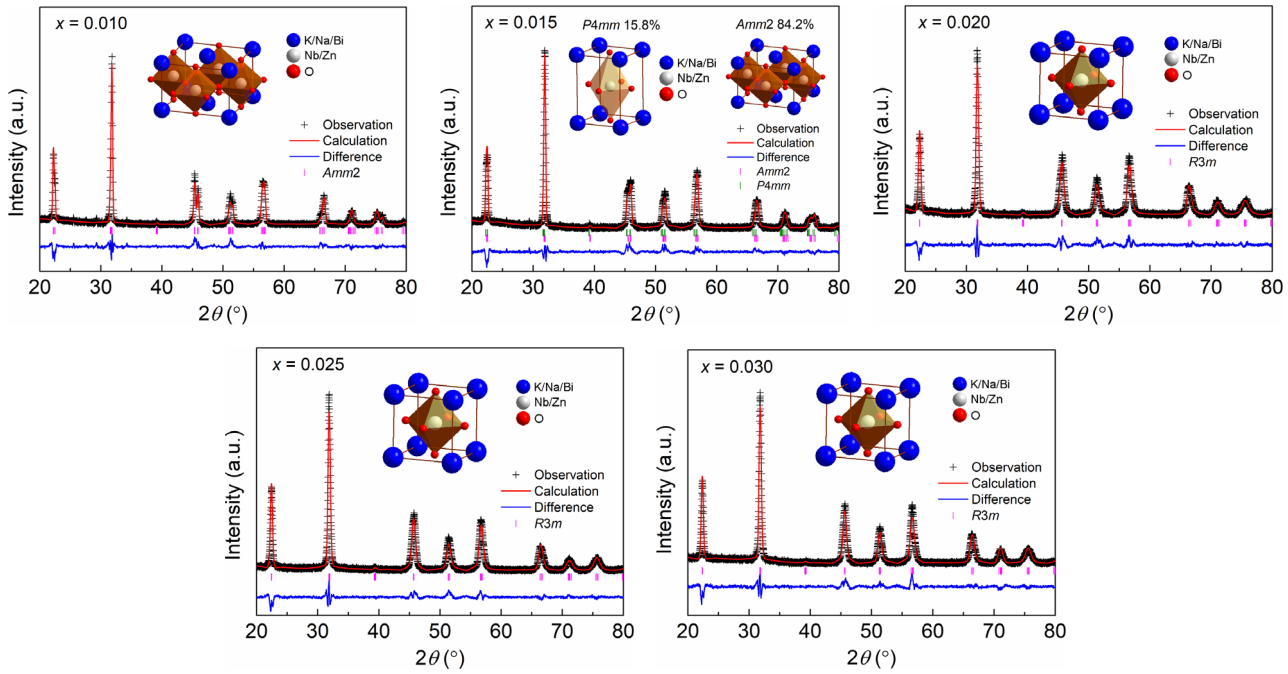

Fig. 2 Rietveld refinements for (1−*x*)KNN−*x*BZN (*x* = 0.010, 0.015, 0.020, 0.025, and 0.030) ceramics at RT.

Table 1 Detailed crystalline parameters, R_{wp}, and R_p factors of Rietveld refinement for (1−*x*)KNN–*x*BZN (*x* = 0.010, 0.015, 0.020, 0.025, and 0.030) ceramics at RT

Composition	*x* = 0.010	*x* = 0.015		*x* = 0.020	*x* = 0.025	*x* = 0.030
Space group	*Amm*2	*Amm*2	*P*4*mm*	*R*3*m*	*R*3*m*	*R*3*m*
Symmetry	Orthorhombic	Orthorhombic	Tetragonal	Rhombohedral	Rhombohedral	Rhombohedral
Phase fraction	100%	84.2%	15.8%	100%	100%	100%
a (Å)	3.95535(20)	3.9606(9)	3.99541(23)	3.98067(11)	3.98027(23)	3.97982(23)
b (Å)	5.6708(4)	5.6471(9)	3.99541(23)	3.98067(11)	3.98027(23)	3.97982(23)
c (Å)	5.6395(4)	5.6494(3)	3.95886(23)	3.98067(11)	3.98027(23)	3.97982(23)
$\alpha/\beta/\gamma$ (°)	90.0	90.0	90.0	90.161(9)	90.168(7)	89.831(8)
V (Å^3)	126.492(17)	126.359(49)	63.197(10)	63.076(5)	63.057(11)	63.036(11)
x (K/Na/Bi)	0.0	0.0	0.0	0.00318	0.00149	0.01849
y (K/Na/Bi)	0.0	0.0	0.0	0.00318	0.00149	0.01849
z (K/Na/Bi)	0.00408	0.0031	0.00869	0.00318	0.00149	0.01849
x (Nb/Zn)	0.5	0.5	0.5	0.52985	0.52776	0.52456
y (Nb/Zn)	0.0	0.0	0.5	0.52985	0.52776	0.52456
z (Nb/Zn)	0.50477	0.47511	0.55059	0.52985	0.52776	0.52456
x (O1)	0.0	0.0	0.5	0.48403	0.48545	0.48656
y (O1)	0.0	0.0	0.5	0.48403	0.48545	0.48656
z (O1)	0.5424	0.51009	0.05124	0.02937	0.03185	0.01835
x (O2)	0.5	0.5	0.5	—	—	—
y (O2)	0.20327	0.20963	0.0	—	—	—
z (O2)	0.19865	0.19067	0.48132	—	—	—
R_{wp} (%)	8.63	8.43		8.18	7.80	7.66
R_p (%)	6.42	6.15		6.27	6.02	5.84

Table 2 Fitting parameters for (1−*x*)KNN–*x*BZN ceramics with different BZN contents based on deviation degree and modified Curie–Weiss law

Composition	*x* = 0.010	*x* = 0.015	*x* = 0.020	*x* = 0.025	*x* = 0.030
T_0 (℃)	360.4(2)	340.8(5)	286.8(0)	234.7(3)	205.7(5)
$C\times10^5$ (℃)	1.45(8)	2.01(6)	2.25(2)	2.31(5)	2.49(4)
T_{CW} (℃)	394.8(3)	418.0(8)	424.0(8)	424.1(4)	424.2(0)
T_m (℃)	393.9(9)	388.3(5)	385.6(7)	365.2(0)	359.6(4)
$\Delta T_m = T_{CW} - T_m$ (℃)	0.8(4)	29.7(3)	38.4(1)	58.9(4)	64.5(6)
γ	1.26(0)	1.48(9)	1.85(4)	1.89(3)	1.89(6)

C reflects the transition nature of ferroelectrics, T_0 is a constant, T_m is temperature at maximal permittivity, T_{CW} is the starting temperature of permittivity deviating from the Curie–Weiss law, and γ describes the diffuse state.

octahedral unit can be obtained: 63.24608 Å^3 for *x* = 0.010, 63.18248 Å^3 for *x* = 0.015, 63.0765 Å^3 for *x* = 0.020, 63.05711 Å^3 for *x* = 0.025, and 63.03611 Å^3 for *x* = 0.030. The volume of octahedral unit declines slowly with the increase of BZN, which is connected with ion substitution. For the (1−*x*)KNN–*x*BZN solid solution, according to the principle of radius match in the ABO_3-type perovskite structure, the larger size K^+ (1.64 Å, coordination number (CN) = 12), Na^+ (1.39 Å, CN = 12), and Bi^{3+} (1.36 Å, CN = 12) locate at the A site, whereas the smaller size Nb^{5+} (0.64 Å, CN = 12) and Zn^{2+} (0.74 Å, CN = 12) enter into the B site [20,28]. As a result, the addition of BZN slightly reduces the volume of octahedral unit. Besides, with increasing BZN content to $0.020 \leqslant x \leqslant 0.030$, the larger size Zn^{2+} replacing Nb^{5+} at the B site produces a great lattice distortion to make the rhombohedral symmetry stable above RT, which agrees with the XRD results.

The SEM micrographs of (1−*x*)KNN–*x*BZN ceramics are displayed in Figs. 3(a)−3(e). The microstructure morphologies show that the samples with $0.010 \leqslant x \leqslant 0.020$ are very dense with well grown grains and few pores (Figs. 3(a)−3(c)). With increasing BZN, a

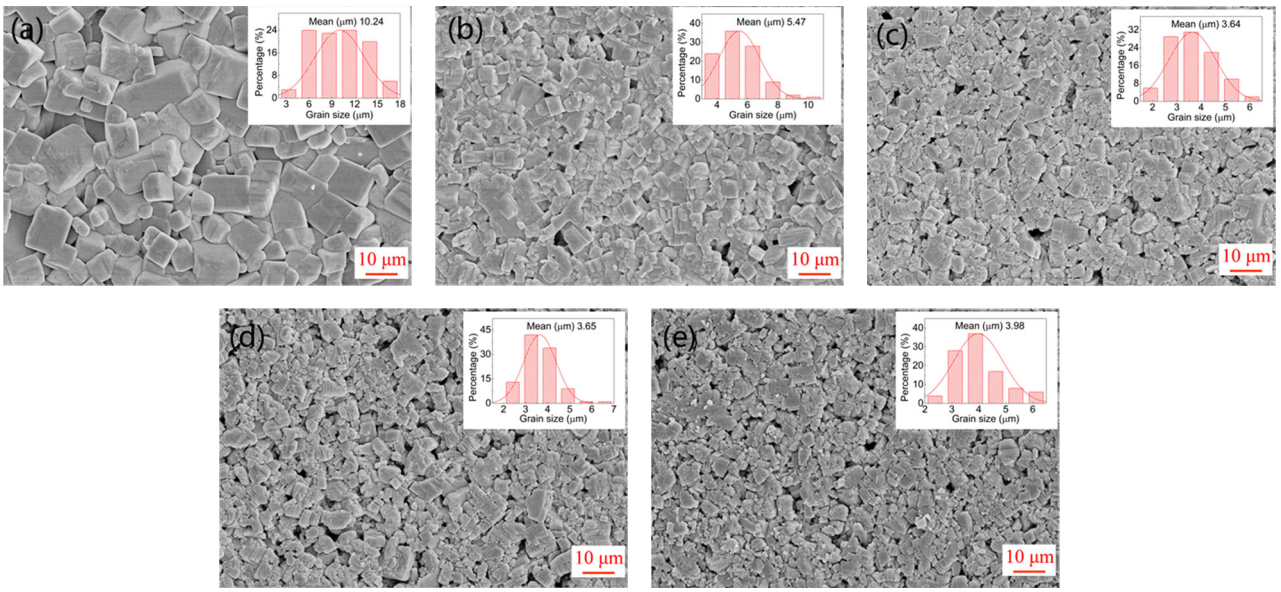

Fig. 3 SEM micrographs of (1−*x*)KNN–*x*BZN ceramics: (a) $x = 0.010$, (b) $x = 0.015$, (c) $x = 0.020$, (d) $x = 0.025$, and (e) $x = 0.030$. The insets show the distribution of grain sizes.

large number of pores and irregular grains are formed for the sample with $x = 0.025$ and 0.030 (Figs. 3(d) and 3(e)). The distribution of grain sizes is measured by ImageJ software and plotted in the insets of Figs. 3(a)−3(e), and the average grain sizes are 10.24, 5.47, 3.64, 3.65, and 3.98 μm for the samples with $x = 0.010$, 0.015, 0.020, 0.025, and 0.030, respectively. In $0.010 \leqslant x \leqslant 0.020$, the average grain size dramatically declines, implying that a small amount of BZN restrains the grain growth. It was reported that the a low concentration of Bi^{3+} can act as a grain inhibitor in the KNN–$(Bi_{0.5}Na_{0.5})TiO_3$ and KNN–$Bi(Zn_{0.75}W_{0.25})O_3$ ceramics [29,30], and thus the decrease of average grain size in this study should be attributed to the role of Bi^{3+}. However, with further increasing BZN content up to $x = 0.025$ and 0.030, the average grain size slightly increases, which could reach a saturation value. In addition, the bulk densities of the samples with $x = 0.010$, 0.015, 0.020, 0.025, and 0.030 are 4.34, 4.32, 4.30, 4.21, and 4.23 g/cm^3, respectively. It can be found that the density of $0.010 \leqslant x \leqslant 0.020$ is much higher than that of $0.025 \leqslant x \leqslant 0.030$ in consistent with the result of microstructure morphologies.

The temperature dependence of ε' of (1−*x*)KNN–*x*BZN ceramics at 1 MHz is plotted in Fig. 4. The sample with $x = 0.010$ exhibits an orthorhombic phase due to the T_m and $T_{O–T}$ permittivity peaks above RT. The inset of Fig. 4 shows that T_m declines rapidly with the addition of BZN. The $T_{O–T}$ around 125 ℃ in the sample with $x = 0.015$ suggests the O–T mixed phase occurring at RT, and a similar phenomenon was also found in the $0.94(K_{0.4-x}Na_{0.6}Ba_xNb_{1-x}Zr_x)O_3$–$0.06LiSbO_3$ solid solution [31]. It is noted that the samples with $x = 0.020$ and $0.025 \leqslant x \leqslant 0.03$ exhibit a step-like feature around 171 and 206 ℃, respectively, which is much higher than the $T_{O–T}$ for the sample with $x = 0.015$. Such a step-like feature is related to the rhombohedral–tetragonal (R–T) phase transition in similarity to the reported KNN-based solid solutions [7,31]. It suggests that a small amount of BZN stabilizes the rhombohedral phase whereas suppresses the orthorhombic phase. The aforementioned dielectric behavior related to the phase transition further verifies the crystal structure, which is in agreement with the XRD analysis and Rietveld refinement. Moreover, the samples with $0.020 \leqslant x \leqslant 0.030$ exhibit a

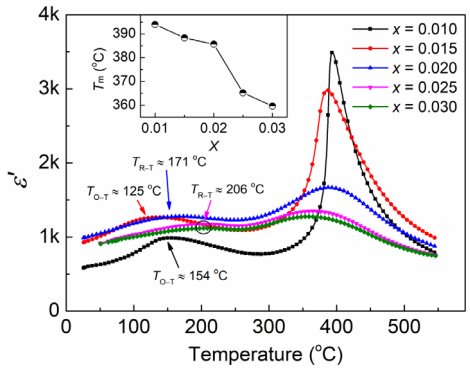

Fig. 4 Temperature dependence of ε' for (1−*x*)KNN–*x*BZN ceramics with different BZN contents at 1 MHz. The inset shows T_m as a function of BZN content (x).

tetragonal–cubic (T–C) diffuse phase transition, which has been frequently reported in the ferroelectrics with relaxor characteristics [16–20]. Consequently, the high-temperature stability of permittivity is greatly enhanced by the combination of R–T step-like feature and the diffuse phase transition from tetragonal to cubic.

The permittivity above Curie temperature (T_C) for typical ferroelectrics generally follows the Curie–Weiss law $1/\varepsilon' = (T - T_0)/C$ ($T > T_C$). Figure 5 displays the temperature dependence of reverse permittivity for (1−x)KNN–xBZN ceramics at 1 MHz. It is obvious that the permittivity for the samples with $0.020 \leqslant x \leqslant 0.030$ deviates from the Curie–Weiss law. The deviation degree can be expressed as $\Delta T_m = T_{CW} - T_m$ [32] (Fig. 5). The linear fitting between reverse permittivity and temperature above T_{CW} is carried out and the fitted parameters are listed in Table 2. The inset of Fig. 5 shows that ΔT_m continuously increases with the addition of BZN, which indicates that introducing BZN gradually improves the diffuse phase transition behavior of the system.

To further quantitatively characterize the diffuse phase transition behavior of permittivity above T_m for (1−x)KNN–xBZN system, the modified Curie–Weiss law proposed by Uchino and Nomura [33] is adopted by the following equation:

$$\frac{1}{\varepsilon'} - \frac{1}{\varepsilon'_m} = \frac{(T - T_m)^\gamma}{C_1} \quad (1)$$

where ε'_m is the maximal permittivity when $T = T_m$, C_1 is a constant on Curie–Weiss behavior, and $\gamma = 1$ and 2 are the classical ferroelectric state and relaxor ferroelectric state, respectively, $1 \leqslant \gamma \leqslant 2$. Figure 6 displays the $\log(1/\varepsilon' - 1/\varepsilon'_m)$ as a function of $\log(T - T_m)$

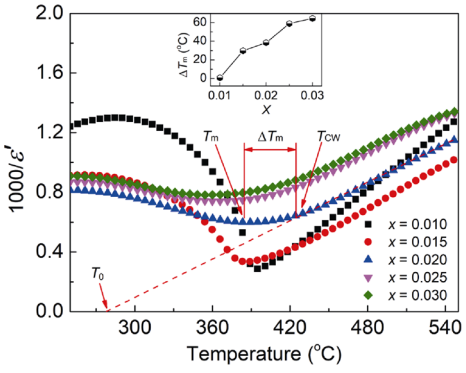

Fig. 5 Temperature dependence of reverse permittivity for (1−x)KNN–xBZN ceramics with different BZN contents at 1 MHz. The inset shows deviation degree (ΔT_m) as a function of BZN content (x).

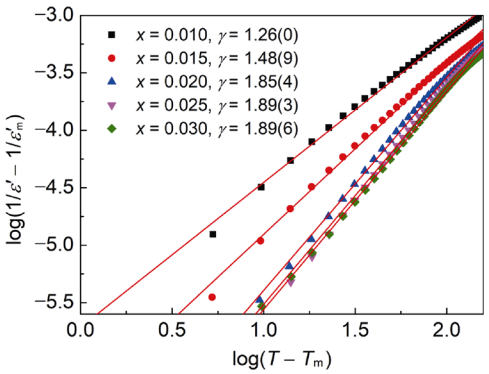

Fig. 6 $\text{Log}(1/\varepsilon' - 1/\varepsilon'_m)$ as a function of $\log(T - T_m)$ of (1−x)KNN–xBZN ceramics with different BZN contents at 1 MHz. The red lines show linear fitting.

for (1−x)KNN–xBZN ceramics at 1 MHz. The linear fitting is conducted as shown by red lines in Fig. 6, the γ can be gained from the fitted slope: $\gamma = 1.260$ for $x = 0.010$, $\gamma = 1.489$ for $x = 0.015$, $\gamma = 1.854$ for $x = 0.020$, $\gamma = 1.893$ for $x = 0.025$, and $\gamma = 1.896$ for $x = 0.030$. With increasing BZN, the γ monotonously increases from 1.260 to 1.893. Especially, the γ values are close to 2 for the samples with $0.020 \leqslant x \leqslant 0.030$, implying a diffuse phase transition behavior associated with the thermal evolution of polar nano-regions (PNRs) size due to ion substitution [34–36]. In this work, since the valence and radius of Bi^{3+} at the A site of ABO_3-type perovskite structure are different from those of K^+, Na^+, and similar cases also appear at the B site. In comparison with the larger size Zn^{2+}, a more pronounced off-center shift for the smaller size Nb^{5+} exists in oxygen octahedra, similar to that has been reported in the $(Bi_{0.5}Li_{0.5})ZrO_3$ and $(Bi_{0.5}Na_{0.5})TiO_3$ modified KNN solid solutions [7,19,34]. Then, the introduction of Bi^{3+} (including a chemically active lone electron pair) into K^+/Na^+ and Zn^{2+} into Nb^{5+} not only interrupts the long-range Nb^{5+} displacement, but also leads to substantial local lattice strain. The mismatches of valence and size produce local static electric and elastic fields, and thereby the ferroelectric long-range order is prevented which results in the formation of PNRs. When the doping content of BZN is not very high, the PNRs are embedded in the lattice matrix of (1−x)KNN–xBZN ceramics, which gives rise to the diffuse phase transition behavior.

The temperature variation of permittivity plays a very important role in practical application of HTCC materials. Figure 7(a) shows the temperature variation of permittivity ($\Delta\varepsilon'/\varepsilon'_{300\,℃}$, $\Delta\varepsilon' = \varepsilon' - \varepsilon'_{300\,℃}$) for (1−$x$)KNN–$x$BZN ceramics at 1 MHz. The addition of

BZN greatly enhances the high-temperature stability of permittivity. According to the ±15% tolerance of Electronic Industries Alliance X8R capacitor standards as shown by the gray flame in Fig. 7(a) [7,8], the samples with x = 0.020, 0.025, and 0.030 show broad high-temperature ranges of 75–342, 103–459, and 96–457 ℃, respectively. In Fig. 7(b), the tanδ of (1−x)KNN–xBZN ceramics as a function of temperature at 1 MHz shows that the tanδ for the samples with x = 0.020 and 0.025 remains low (⩽ 0.05) in broad temperature ranges of 79–433 and 119–364 ℃, respectively, but it only exists a narrow temperature range of 137–326 ℃ for the sample with x = 0.030. Therefore, 0.98KNN–0.02BZN ceramic with a stable ε' (≈ 1310, ±15% tolerance) and a low tanδ (⩽ 5%) from 79 to 342 ℃, and 0.975KNN–0.025BZN ceramic with a stable ε' (≈ 1219, ±15% tolerance) and a low tanδ (⩽ 5%) from 119 to 364 ℃, are the potential materials for HTCC application. It is noted that the introduction of BZN greatly enhances the high-temperature tanδ due to the thermally activated conductivity behavior [37–39].

To better understand the influence of BZN content on the high-temperature conductivity behavior of the system, the normalized imaginary parts of impedance (Z''/Z''_{max}) for (1−x)KNN–xBZN ceramics as a function of frequency at selected temperatures are shown in Figs. 8(a)−8(e). A systematic loss peak exhibits at the measuring frequency region. With increasing temperature, the peak frequency (relaxation frequency, f_{max}) moves toward high frequency, which indicates a thermally activated relaxation behavior [39–41]. This relaxation behavior indicates that elevating temperature accelerates

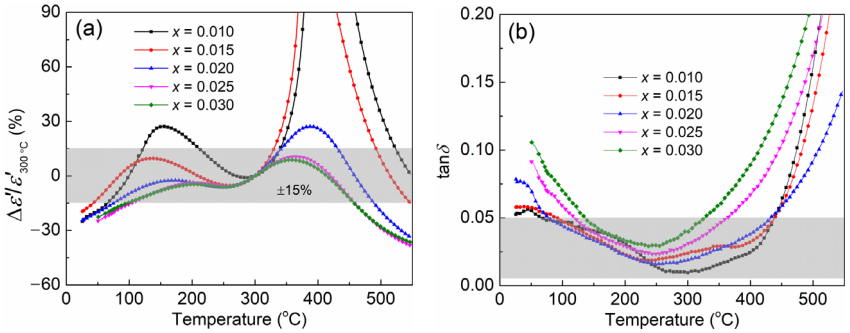

Fig. 7 Temperature variation of (a) ε' and (b) tanδ as a function of temperature for (1−x)KNN–xBZN (x = 0.010, 0.015, 0.020, 0.025, and 0.030) ceramics at 1 MHz.

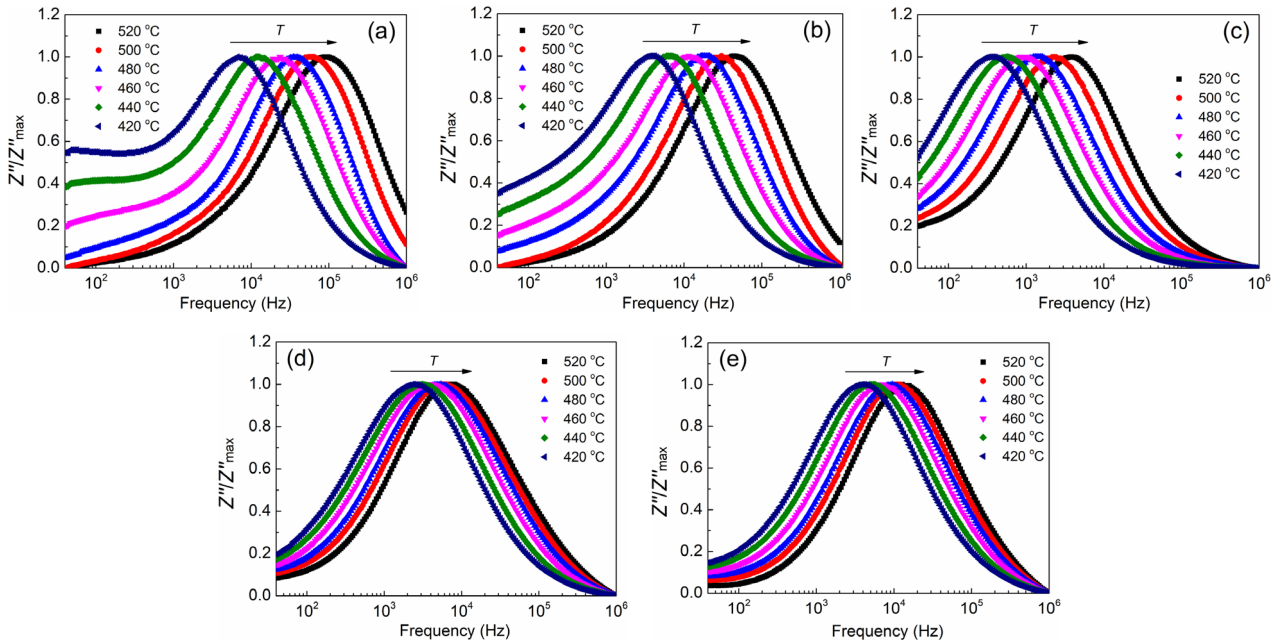

Fig. 8 Normalized imaginary parts of impedance (Z''/Z''_{max}) for (1−x)KNN–xBZN ceramics as a function of frequency at selected temperatures: (a) x = 0.010, (b) x = 0.015, (c) x = 0.020, (d) x = 0.025, and (e) x = 0.030.

the hopping or migration of charge carriers (electrons, holes, and ions). The relationship between f_{max} and temperature can be established by the following equation (Arrhenius law):

$$f_{max} = f_0 \exp\left(\frac{-E_{rel}}{k_B T}\right) \quad (2)$$

where f_0 is a constant on relaxation behavior, E_{rel} represents the activation energy on relaxation behavior, k_B and T are the Boltzmann constant (eV/K) and absolute temperature (K), respectively. By fitting the Arrhenius plots of relaxation frequency as shown by the red lines in Fig. 9, the E_{rel} can be determined according to the fitted slope: E_{rel} = 1.240 eV for x = 0.010, E_{rel} = 1.154 eV for x = 0.015, E_{rel} = 1.095 eV for x = 0.020, E_{rel} = 0.596 eV for x = 0.025, and E_{rel} = 0.555 eV for x = 0.030. The E_{rel} monotonously declines with increasing BZN.

The frequency dependence of AC conductivity (σ_{AC}) for (1−x)KNN–xBZN ceramics at selected temperatures is displayed in Figs. 10(a)−10(e). With the increase of frequency, the σ_{AC} first exhibits a low-frequency platform that is close to DC conductivity (σ_{DC}) and then dramatically increases due to the contribution of localized charge carriers by hopping or migration to conductivity. The conductivity behavior describes the many-body mutual actions between dipoles and charge carriers. It can be established by the following equation

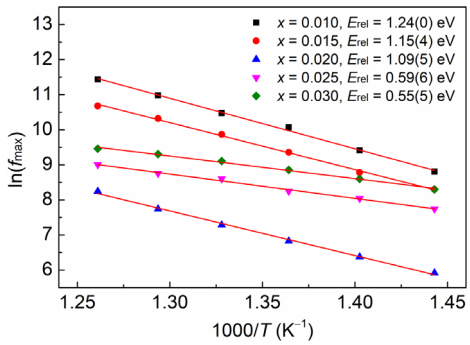

Fig. 9 Arrhenius plots of relaxation frequency for (1−x)KNN–xBZN ceramics with different BZN contents. The red lines show linear fitting.

("universal dielectric response" (UDR) law [40,41]):

$$\sigma_{AC} = \sigma_{DC} + \sigma_0 f^s \quad (3)$$

where σ_0, f, and s are a constant on σ_{AC}, the measuring frequency, and a frequency exponent ($0 < s \leqslant 1$), respectively. The σ_{DC} can be determined by the nonlinear fitting between σ_{AC} and frequency based on Eq. (3), as shown by the red lines in Fig. 10. The relationship between σ_{DC} and temperature can be described based on the the following equation (Arrhenius law):

$$\sigma_{DC} = \sigma_1 \exp\left(-\frac{E_{con}}{k_B T}\right) \quad (4)$$

where σ_1 is a constant on σ_{DC} and E_{con} represents the

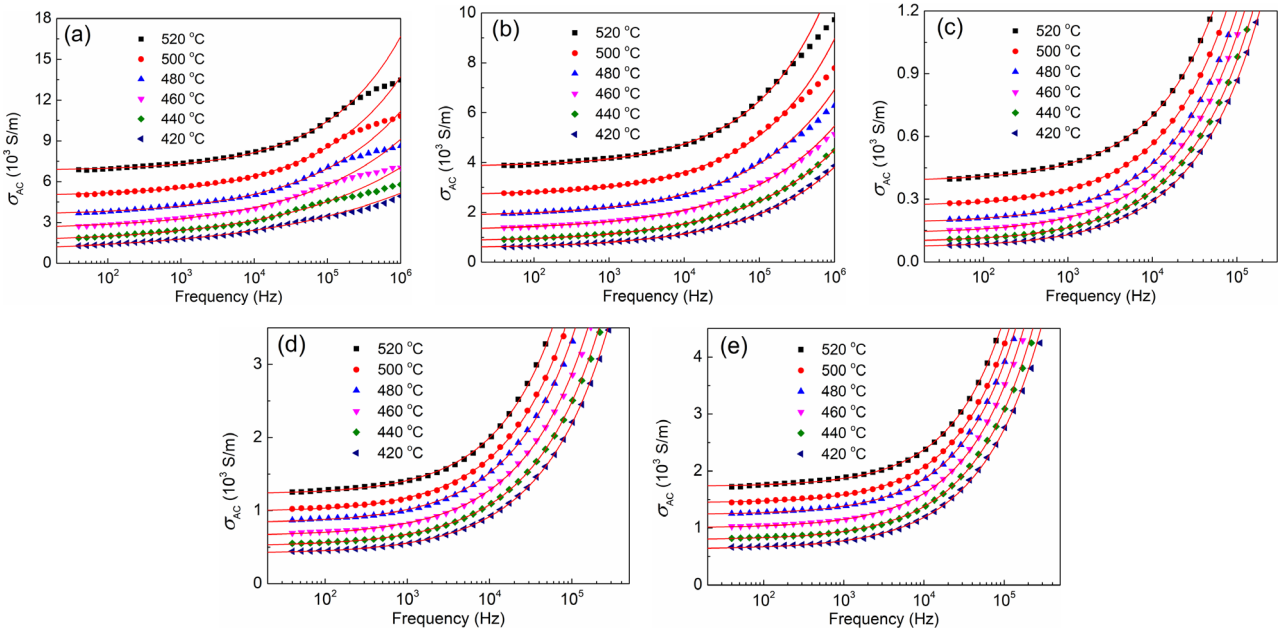

Fig. 10 Frequency dependent σ_{AC} of (1−x)KNN–xBZN ceramics at selected temperatures: (a) x = 0.010, (b) x = 0.015, (c) x = 0.020, (d) x = 0.025, and (e) x = 0.030. The red lines show nonlinear fitting based on Eq. (3).

activation energy on σ_{DC}. By fitting the Arrhenius plots of σ_{DC} as shown by the red lines in Fig. 11, the E_{con} can be determined according to the fitted slope: E_{con} = 1.064 eV for x = 0.010, E_{con} = 0.983 eV for x = 0.015, E_{con} = 0.873 eV for x = 0.020, E_{con} = 0.582 eV for x = 0.025, and E_{con} = 0.543 eV for x = 0.030. The variation of E_{con} is in agreement with that of E_{rel}. Moreover, the E_{rel} values of all the samples are greater than those of E_{con}. This is due to that E_{rel} equals the free energy of charge carriers by hopping or migration between adjacent lattice sites whereas the E_{con} involves both the long-distance hopping/migration free energy of charge carriers and the creation of charge carriers [42,43]. Therefore, the difference between them is associated with the creation of free energy, which indicates that charge carriers (electrons, holes, and ions) are dissociated from the traps and defects exist in the samples.

In perovskite oxides, oxygen vacancies are one of the most common charged carriers and have a crucial effect on the high-temperature conductivity behavior. It was reported that the activation energy of single-ionized oxygen vacancies is in the range of 0.3–0.5 eV and it is 0.6–1.2 eV for that of doubly-ionized oxygen vacancies [44]. According to the magnitude of E_{con} and E_{rel}, the charged carriers in (1−x)KNN–xBZN ceramics are considered to be doubly-ionized oxygen vacancies. Generally, the volatilization of K/Na/Bi from the lattice during sintering could be compensated by oxygen vacancies. In addition, the possible Nb^{5+} substitution by Zn^{4+} generates the defect dipoles with regard to the acceptor ions and the charge compensation of oxygen vacancies. The corresponding Kroger–Vink notations can be expressed as the following equations:

$$A_A \rightarrow A + V'_A + 0.5V_O^{\bullet\bullet} \quad (5)$$

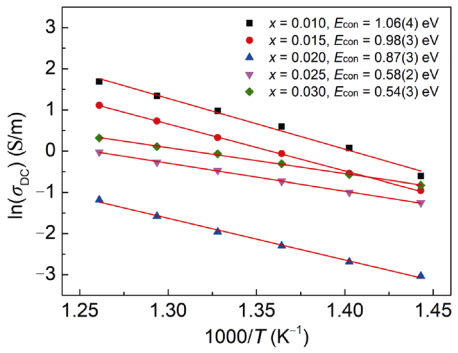

Fig. 11 Arrhenius plots of σ_{DC} for (1−x)KNN–xBZN ceramics with different BZN contents. The red lines show linear fitting.

$$Bi_{Bi} \rightarrow Bi + V'''_{Bi} + 1.5V_O^{\bullet\bullet} \quad (6)$$

$$Zn_{Zn}^{4+} \rightarrow Zn'_{Nb} + 0.5V_O^{\bullet\bullet} \quad (7)$$

where V'_A, V'''_{Bi}, Zn'_{Nb}, and $V_O^{\bullet\bullet}$ are the K/Na vacancy, Bi vacancy, quadruple ionized Zn^{4+} locating at the Nb^{5+} site, and doubly-ionized oxygen vacancy, respectively. Equations (5)−(7) show that both the formation of Bi vacancy and creation of negatively charged defect Zn'_{Nb} produce oxygen vacancies. Thus, the addition of BZN enhances the concentration of oxygen vacancies, allowing activation energy to be reduced, which agrees with the variation of E_{con} and E_{rel}. It is noted that with increasing BZN, both E_{rel} and E_{con} initially decrease slightly, then drop sharply at x = 0.025, and finally decline slowly. The change of activation energy generally depends on the concentration of oxygen vacancies, lattice distortion, and microstructure morphologies [20–22]. Since the volume change of octahedral unit for (1−x)KNN–xBZN system is almost independent of BZN content, it is assumed that such a decrease of activation energy could be related to microstructure morphologies and the concentration of oxygen vacancies. With the increase of BZN, all the samples with $0.010 \leqslant x \leqslant 0.020$ are dense and the higher concentration of oxygen vacancies plays a major role in the slight decrease of activation energy. For the sample with x = 0.025, the formation of a large number of pores provides the large surface on the grains to make activation energy of oxygen vacancies decreased greatly [42]. Further increasing BZN content up to x = 0.030, the microstructure morphology is almost unchanged and the slight decrease of activation energy is associated with the improvement of oxygen vacancy concentration.

4 Conclusions

(1−x)KNN–xBZN ceramics were fabricated via the traditional solid-state method. The crystal structure, microstructure, dielectric, and conductivity behavior of the system were investigated systematically. The crystal structure dependence of BZN was determined by XRD patterns, Rietveld refinement, and dielectric spectroscopy. The decrease of octahedral unit is associated with the ion substitution. Due to the combination of R–T step-like feature and T–C diffuse phase transition, 0.98KNN–0.02BZN ceramic exhibits a stable ε' ($\approx$ 1310, ±15% tolerance) and a low tanδ

(⩽ 5%) in a broad temperature range of 79–342 ℃. In addition, a stable ε' (≈ 1219, ±15% tolerance) and a low tanδ (⩽ 5%) from 119 to 364 ℃ are obtained for 0.975KNN–0.025BZN ceramic. The activation energies of dielectric relaxation and conductivity behavior at high temperatures initially decrease slightly, then drop sharply, and finally decline slowly, which could be attributed to microstructure morphologies and the concentration of oxygen vacancies.

Acknowledgements

This work was supported by the Natural Science Foundation of Guangxi (Grant Nos. 2019GXNSFBA245069, AA138162, GA245006, and AA294014), the Middle-aged and Young Teachers' Basic Ability Promotion Project of Guangxi (Grant No. 2019KY0290), the Guilin University of Technology (Grant No. GUTQDJJ20176612037), the High Level Innovation Team and Outstanding Scholar Program of Guangxi Institutes, the Open Research Program of Key Laboratory of RF Circuit and System, Ministry of Education, and the Key Laboratory of Large Scale Integrated Design of Zhejiang.

References

[1] Watson J, Castro G. A review of high-temperature electronics technology and applications. *J Mater Sci: Mater Electron* 2015, **26**: 9226–9235.

[2] Ren PR, He JJ, Yan FX, *et al*. Temperature-stable dielectric and energy storage properties of $(1-x)(0.94Bi_{0.5}Na_{0.5}TiO_3–0.09BiAlO_3)–xSrTiO_3$ ceramics. *J Alloys Compd* 2019, **807**: 151676.

[3] Chen Z, Li GZ, Sun XJ, *et al*. La_2O_3 modified $0.4(Ba_{0.8}Ca_{0.2})TiO_3–0.6Bi(Mg_{0.5}Ti_{0.5})O_3$ ceramics for high-temperature capacitor applications. *Ceram Int* 2015, **41**: 11057–11061.

[4] Hirose S, Usui T, Crossley S, *et al*. Progress on electrocaloric multilayer ceramic capacitor development. *APL Mater* 2016, **4**: 064105.

[5] Kishi H, Mizuno Y, Chazono H. Base-metal electrode-multilayer ceramic capacitors: Past, present and future perspectives. *Jpn J Appl Phys* 2003, **42**: 1–15.

[6] Kobayashi K, Ryu M, Doshida Y, *et al*. Novel high-temperature antiferroelectric-based dielectric $NaNbO_3–NaTaO_3$ solid solutions processed in low oxygen partial pressures. *J Am Ceram Soc* 2013, **96**: 531–537.

[7] Yan TX, Han FF, Ren SK, *et al*. Dielectric properties of $(K_{0.5}Na_{0.5})NbO_3–(Bi_{0.5}Li_{0.5})ZrO_3$ lead-free ceramics as high-temperature ceramic capacitors. *Appl Phys A* 2018, **124**: 338.

[8] Chen XL, Yan X, Li XX, *et al*. Excellent temperature stability on relative permittivity, and conductivity behavior of $K_{0.5}Na_{0.5}NbO_3$ based lead free ceramics. *J Alloys Compd* 2018, **762**: 697–705.

[9] Lin Y, Zhang YJ, Zhan SL, *et al*. Synergistically ultrahigh energy storage density and efficiency in designed sandwich-structured poly(vinylidene fluoride)-based flexible composite films induced by doping $Na_{0.5}Bi_{0.5}TiO_3$ whiskers. *J Mater Chem A* 2020, **8**: 23427–23435.

[10] Lin Y, Li D, Zhang M, *et al*. Excellent energy-storage properties achieved in $BaTiO_3$-based lead-free relaxor ferroelectric ceramics via domain engineering on the nanoscale. *ACS Appl Mater Interaces* 2019, **11**: 36824–36830.

[11] Li D, Lin Y, Zhang M, *et al*. Achieved ultrahigh energy storage properties and outstanding charge-discharge performances in $(Na_{0.5}Bi_{0.5})_{0.7}Sr_{0.3}TiO_3$-based ceramics by introducing a linear additive. *Chem Eng J* 2020, **392**: 123729.

[12] Ogihara H, Randall CA, Trolier-Mckinstry S. Weakly coupled relaxor behavior of $BaTiO_3–BiScO_3$ ceramics. *J Am Ceram Soc* 2009, **92**: 110–118.

[13] Muhammad R, Iqbal Y, Reaney IM. $BaTiO_3–Bi(Mg_{2/3}Nb_{1/3})O_3$ ceramics for high-temperature capacitor applications. *J Am Ceram Soc* 2016, **99**: 2089–2095.

[14] Acosta M, Zang JD, Jo W, *et al*. High-temperature dielectrics in $CaZrO_3$ modified $Bi_{1/2}Na_{1/2}TiO_3$-based lead-free ceramics. *J Eur Ceram Soc* 2012, 32: 4327–4334.

[15] Zeb A, Jan SU, Bamiduro F, *et al*. Temperature-stable dielectric ceramics based on $Na_{0.5}Bi_{0.5}TiO_3$. *J Eur Ceram Soc* 2018, **38**: 1548–1555.

[16] Du HL, Zhou WC, Luo F, *et al*. Phase structure, dielectric properties, and relaxor behavior of $(K_{0.5}Na_{0.5})NbO_3–(Ba_{0.5}Sr_{0.5})TiO_3$ lead-free solid solution for high temperature applications. *J Appl Phys* 2009, **105**: 124104.

[17] Cheng HL, Zhou WC, Du HL, *et al*. Enhanced dielectric relaxor properties in $(1-x)(K_{0.5}Na_{0.5})NbO_3–x(Ba_{0.6}Sr_{0.4})_{0.7}Bi_{0.2}TiO_3$ lead-free ceramic. *J Alloys Compd* 2013, **579**: 192–197.

[18] Chen XL, Wang YL, Chen J, *et al*. Dielectric properties and impedance analysis of $K_{0.5}Na_{0.5}NbO_3–Ba_2NaNb_5O_{15}$ ceramics with good dielectric temperature stability. *J Am Ceram Soc* 2013, **96**: 3489–3493.

[19] Liu LJ, Knapp M, Ehrenberg H, *et al*. Average vs. local structure and composition property phase diagram of $K_{0.5}Na_{0.5}NbO_3–Bi_{1/2}Na_{1/2}TiO_3$ system. *J Eur Ceram Soc* 2017, **37**: 1387–1399.

[20] Yan TX, Ren SK, Ma X, *et al*. Dielectric properties of $(Bi_{0.5}K_{0.5})ZrO_3$ modified $(K_{0.5}Na_{0.5})NbO_3$ ceramics as high temperature ceramic capacitors. *J Electron Mater* 2018, **47**: 7106–7113.

[21] Du HL, Zhou WC, Luo F, *et al*. High T_m lead-free relaxor ferroelectrics with broad temperature usage range: $0.04BiScO_3–0.96(K_{0.5}Na_{0.5})NbO_3$. *J Appl Phys* 2008, **104**: 044104.

[22] Cheng HL, Du HL, Zhou WC, *et al*. $Bi(Zn_{2/3}Nb_{1/3})O_3$–$(K_{0.5}Na_{0.5})NbO_3$ high-temperature lead-free ferroelectric ceramics with low capacitance variation in a broad temperature usage range. *J Am Ceram Soc* 2013, **96**: 833–837.

[23] Liu ZY, Fan HQ, Li MM. High temperature stable dielectric properties of $(K_{0.5}Na_{0.5})_{0.985}Bi_{0.015}Nb_{0.99}Cu_{0.01}O_3$ ceramics with core-shell microstructures. *J Mater Chem C* 2015, **3**: 5851–5858.

[24] Zuo RZ, Fang XS, Ye C. Phase structures and electrical properties of new lead-free $(Na_{0.5}K_{0.5})NbO_3$–$(Bi_{0.5}Na_{0.5})TiO_3$ ceramics. *Appl Phys Lett* 2007, **90**: 092904.

[25] Long CB, Li TY, Fan HQ, *et al*. Li-substituted $K_{0.5}Na_{0.5}NbO_3$-based piezoelectric ceramics: Crystal structures and the effect of atmosphere on electrical properties. *J Alloys Compd* 2016, **658**: 839–847.

[26] Wang RP, Itoh M. Phase diagram of $(Na_{0.5}K_{0.5})NbO_3$–$(Bi_{0.5}Na_{0.5})ZrO_3$ solid solution. *J Adv Dielect* 2016, **6**: 1650014.

[27] Hewat AW. Cubic-tetragonal-orthorhombic-rhombohedral ferroelectric transitions in perovskite potassium niobate: Neutron powder profile refinement of the structures. *J Phys C: Solid State Phys* 1973, **6**: 2559–2572.

[28] Shannon RD. Revised effective ionic radii and systematic studies of interatomic distances in halides and chalcogenides. *Acta Crystallogr Sect A* 1976, **32**: 751–767.

[29] Du HL, Zhou WC, Zhu DM, *et al*. Sintering characteristic, microstructure, and dielectric relaxor behavior of $(K_{0.5}Na_{0.5})NbO_3$–$(Bi_{0.5}Na_{0.5})TiO_3$ lead-free ceramics. *J Am Ceram Soc* 2008, **91**: 2903–2909.

[30] Chen XL, Chen J, Ma DD, *et al*. High relative permittivity, low dielectric loss and good thermal stability of novel $(K_{0.5}Na_{0.5})NbO_3$–$Bi(Zn_{0.75}W_{0.25})O_3$ solid solution. *Mater Lett* 2015, **145**: 247–249.

[31] Liang WF, Wu WJ, Xiao DQ, *et al*. Construction of new morphotropic phase boundary in $0.94(K_{0.4-x}Na_{0.6}Ba_xNb_{1-x}Zr_x)O_3$–$0.06LiSbO_3$ lead-free piezoelectric ceramics. *J Mater Sci* 2011, **46**: 6871–6876.

[32] Guo YP, Kakimoto KI, Ohsato H. Dielectric and piezoelectric properties of lead-free $(Na_{0.5}K_{0.5})NbO_3$–$SrTiO_3$ ceramics. *Solid State Commun* 2004, **129**: 279–284.

[33] Uchino K, Nomura S. Critical exponents of the dielectric constants in diffused-phase-transition crystals. *Ferroelectrics* 1982, **44**: 55–61.

[34] Liu LJ, Knapp M, Ehrenberg H, *et al*. The phase diagram of $K_{0.5}Na_{0.5}NbO_3$–$Bi_{1/2}Na_{1/2}TiO_3$. *J Appl Crystallogr* 2016, **49**: 574–584.

[35] Liu LJ, Knapp M, Schmitt LA, *et al*. Structure and dielectric dispersion in cubic-like $0.5K_{0.5}Na_{0.5}NbO_3$–$0.5Na_{1/2}Bi_{1/2}TiO_3$ ceramic. *EPL Europhys Lett* 2016, **114**: 47011.

[36] Bokov AA, Ye ZG. Recent progress in relaxor ferroelectrics with perovskite structure. *J Mater Sci* 2006, **41**: 31–52.

[37] Wu JG, Wang J. Ferroelectric and impedance behavior of La- and Ti-codoped $BiFeO_3$ thin films. *J Am Ceram Soc* 2010, **93**: 2795–2803.

[38] Wu JG, Xiao DQ, Zhu JG. Potassium-sodium niobate lead-free piezoelectric materials: Past, present, and future of phase boundaries. *Chem Rev* 2015, **115**: 2559–2595.

[39] Yan TX, Sun XJ, Deng JM, *et al*. Dielectric and conductivity behavior of Mn-doped $K_{0.5}Na_{0.5}NbO_3$ single crystal. *Solid State Commun* 2017, **264**: 1–5.

[40] Boukriba M, Sediri F, Gharbi N. Hydrothermal synthesis and electrical properties of $NaNbO_3$. *Mater Res Bull* 2013, **48**: 574–580.

[41] Liu LJ, Wu MX, Huang YM, *et al*. Frequency and temperature dependent dielectric and conductivity behavior of $0.95(K_{0.5}Na_{0.5})NbO_3$–$0.05BaTiO_3$ ceramic. *Mater Chem Phys* 2011, **126**: 769–772.

[42] Li TY, Fan HQ, Long CB, *et al*. Defect dipoles and electrical properties of magnesium B-site substituted sodium potassium niobates. *J Alloys Compd* 2014, **609**: 60–67.

[43] Abdelkafi Z, Abdelmoula N, Khemakhem H, *et al*. Dielectric relaxation in $BaTi_{0.85}(Fe_{1/2}Nb_{1/2})_{0.15}O_3$ perovskite ceramic. *J Appl Phys* 2006, **100**: 114111.

[44] Liu LJ, Fan HQ, Fang L, *et al*. Effects of Na/K evaporation on electrical properties and intrinsic defects in $Na_{0.5}K_{0.5}NbO_3$ ceramics. *Mater Chem Phys* 2009, **117**: 138–141.